Appendix A: Data reduction

We list our estimate of the cross-calibration factor between NIRCam and NIRSpec in Table A.1 and details about the extraction apertures employed for the five template spectra in Table A.2. The cut employed in the paper connects coordinates (5:35:20.0785, -5:24:57.885) and (5:35:21.0801, -5:25:31.157) (α, δ (ICRS, J2000))[32].

Table A.1. NIRSpec/NIRCam cross-calibration measurements.

Filter	a [(1)]	b [(1)] MJy sr^{-1}
(1)	(2)	(3)
g235h-f170lp		
F187N	0.994±0.001	−19.115±1.150
F210M	0.897±0.003	5.252±0.292
F212N	0.804±0.007	13.579±0.474
Average	0.9797±0.0011	6.3578±0.2432
g395h-f290lp		
F335M	0.8709±0.0009	4.6709±0.4649
F405N	0.9213±0.0038	1.8698±2.6086
Average	0.8992±0.0005	3.0398±0.1748

Notes. [(1)]Cross-calibration is parameterised by $I_\nu^{\rm NIRCam} = aI_\nu^{\rm NIRSpec} + b$. We multiply the F100LP and F170LP cubes by the average value of a for F170LP, and we multiply the F290LP cubes by the average value of a for that grating/filter combination. We do not use b in our analysis.

Table A.2. Extraction apertures used in this paper[33].

Template	Center		Size	PA	Projected distance of centre to θ^1 Ori C	
	α (J2000)	δ (J2000)	″×″	°	pc	″
H II region	5:35:20.1545	-5:24:59.646	1.26×2.5	43.738	0.224	111.4
atomic PDR	5:35:20.2307	-5:25:02.555	1.7×2.5	43.738	0.230	114.5
DF 1	5:35:20.5105	-5:25:11.931	1.0×1.6	50.000	0.250	124.7
DF 2	5:35:20.6135	-5:25:14.691	1.0×1.6	38.000	0.257	127.8
DF 3	5:35:20.7095	-5:25:20.351	1.0×2.654	38.000	0.268	133.5

[32] See acknowledgments for data availability.
[33] See acknowledgments for data availability.

Appendix B: Template spectra

The spectral inventory of the five template spectra is shown in Fig. B.1. Line intensities are given in Table B.1, only available in electronic form at the CDS. Column 1 lists the line identification, Column 2 the wavelength in vacuum (μm), Columns 3-17 the wavelength of the peak position of the Gaussian fit, the integrated line intensities and their fit uncertainties in the five templates (in units of erg $cm^{-2}s^{-1}sr^{-1}$). An intensity cutoff of 1×10^{-6} erg cm^{-2} s^{-1} sr^{-1} is applied. We did *not* apply a 3-sigma detection cutoff.

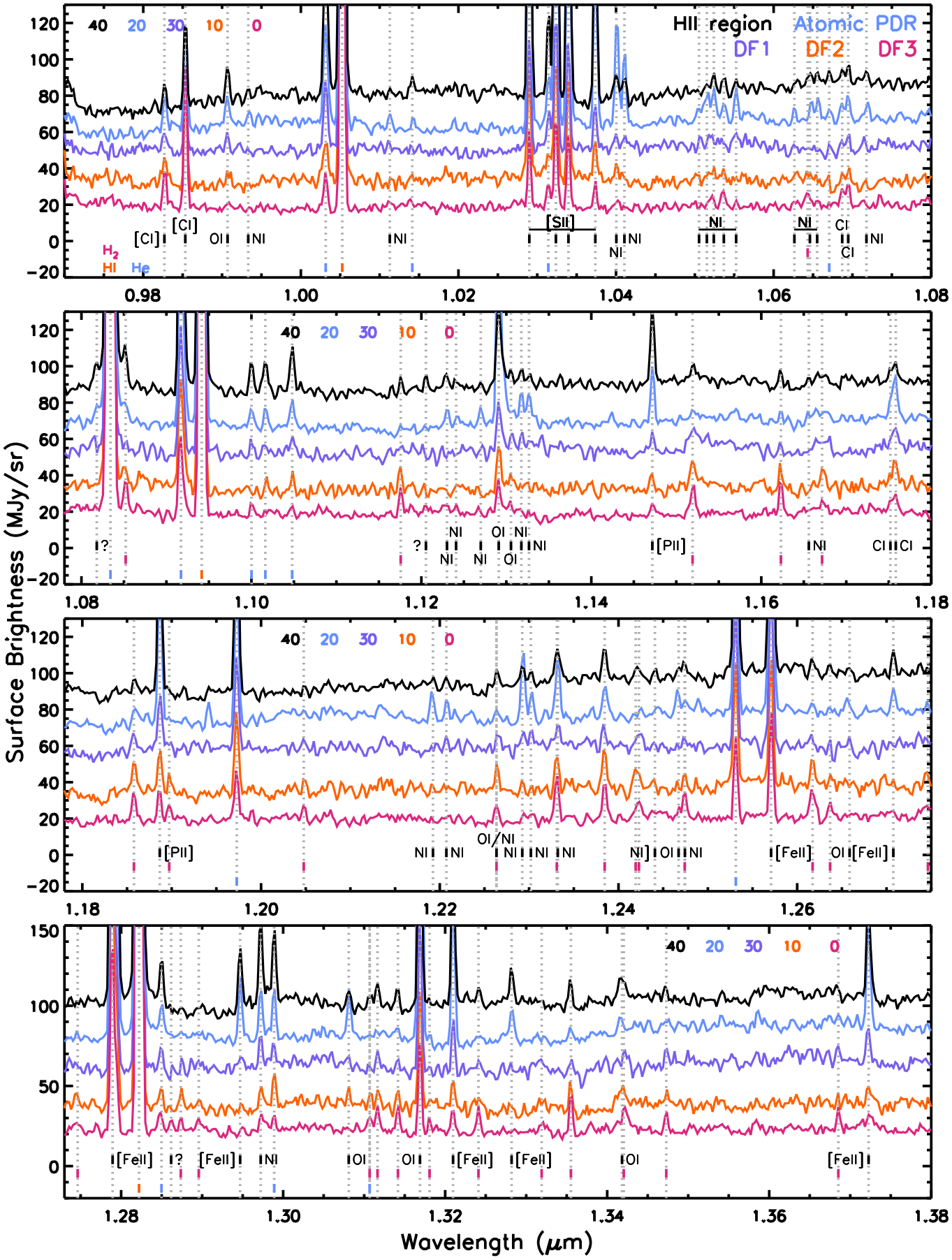

Fig. B.1. Spectral inventory of the five template spectra. Spectra are offset by the numbers given at the top of the panel. Areas susceptible to the wavelength gap are shown in light grey. The colour coding is labelled in the top panel.

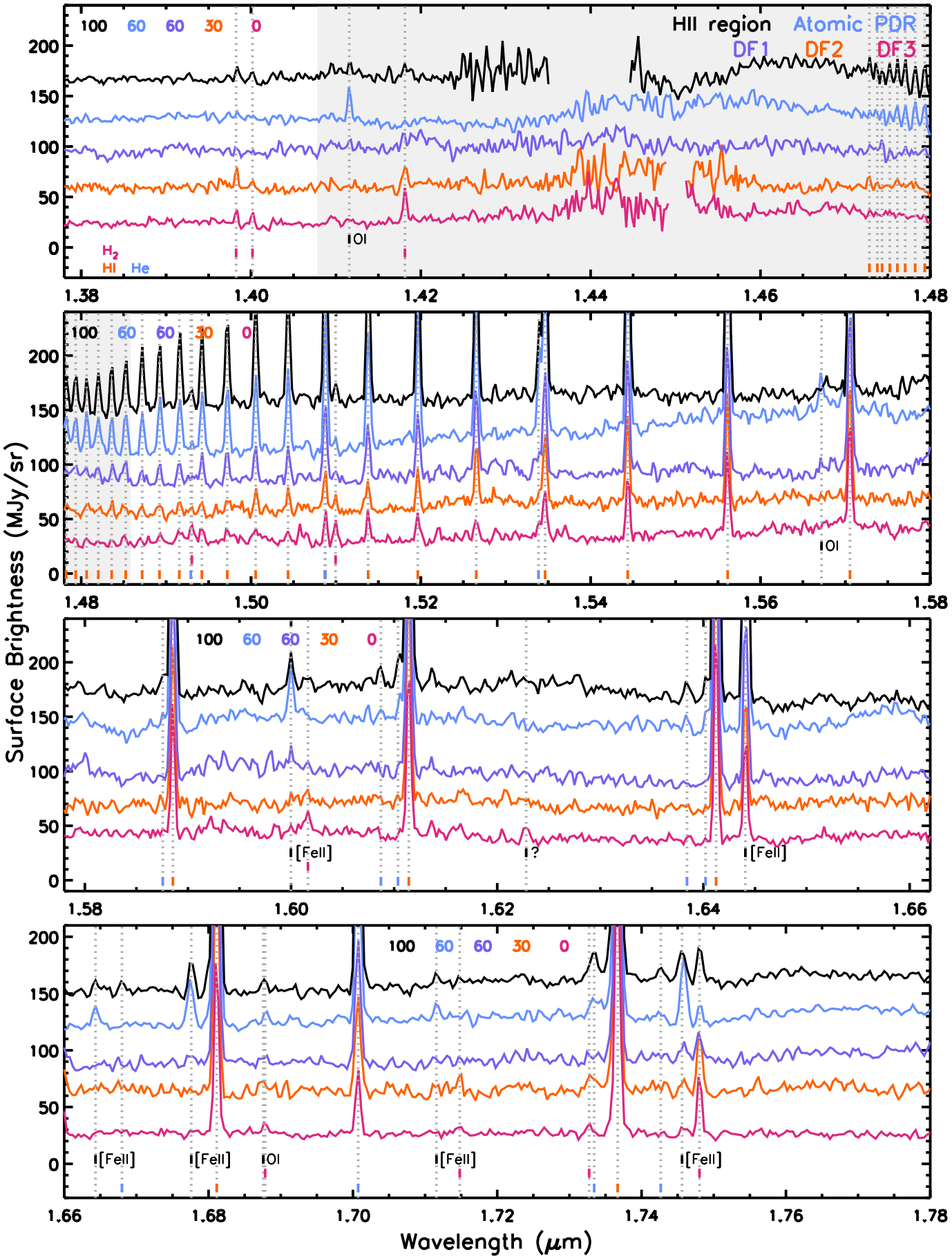

Fig. B.1. continued.

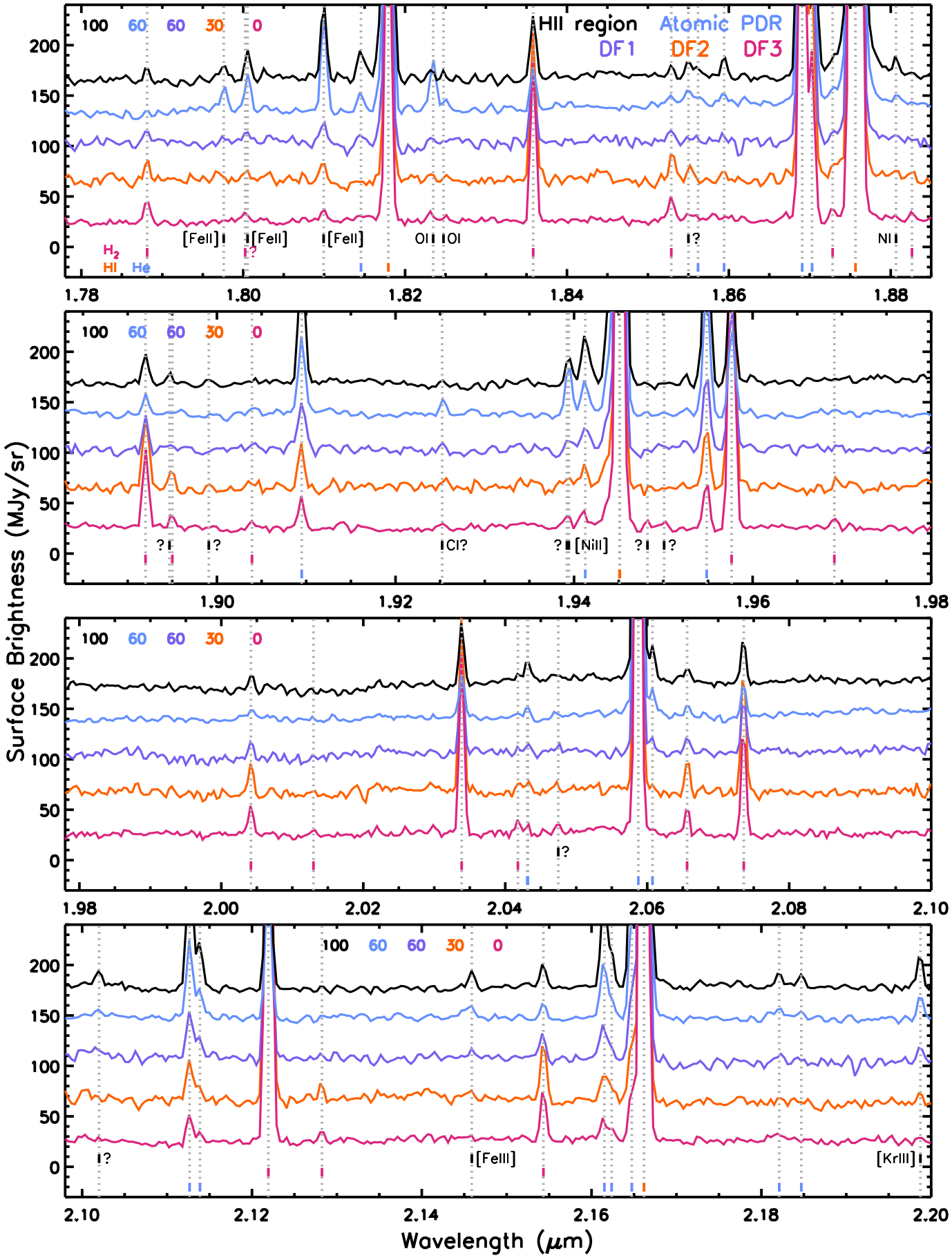

Fig. B.1. continued.

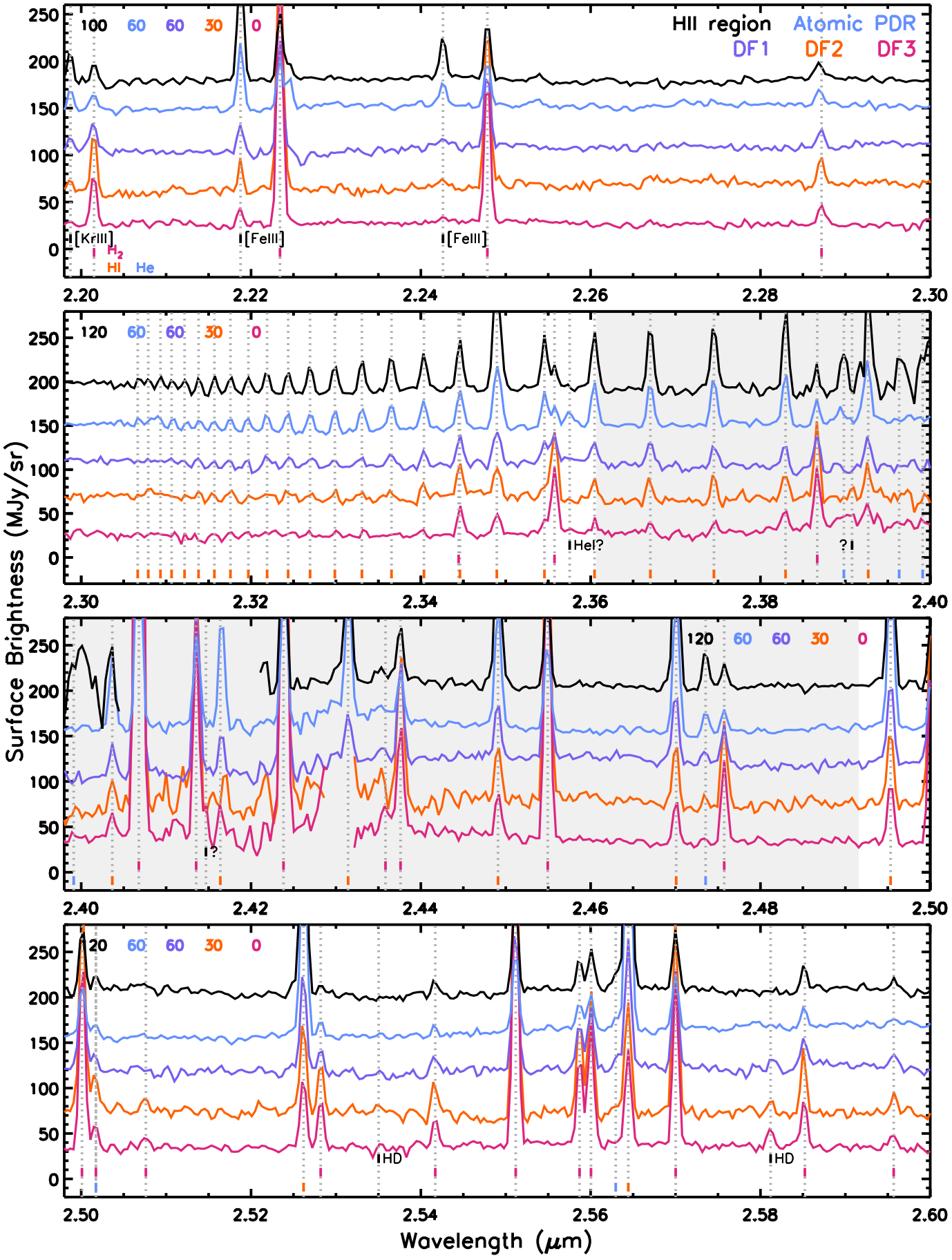

Fig. B.1. continued.

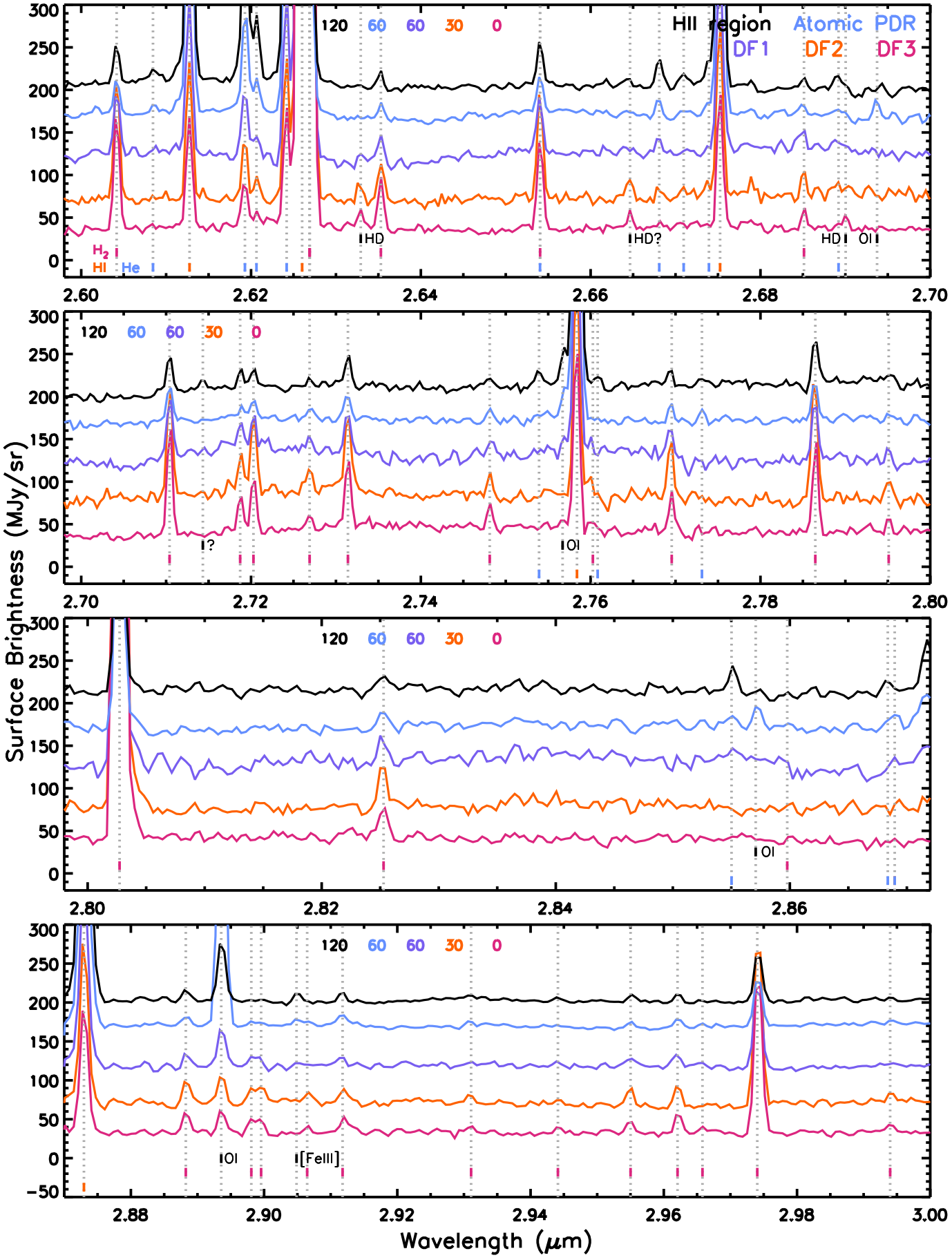

Fig. B.1. continued.

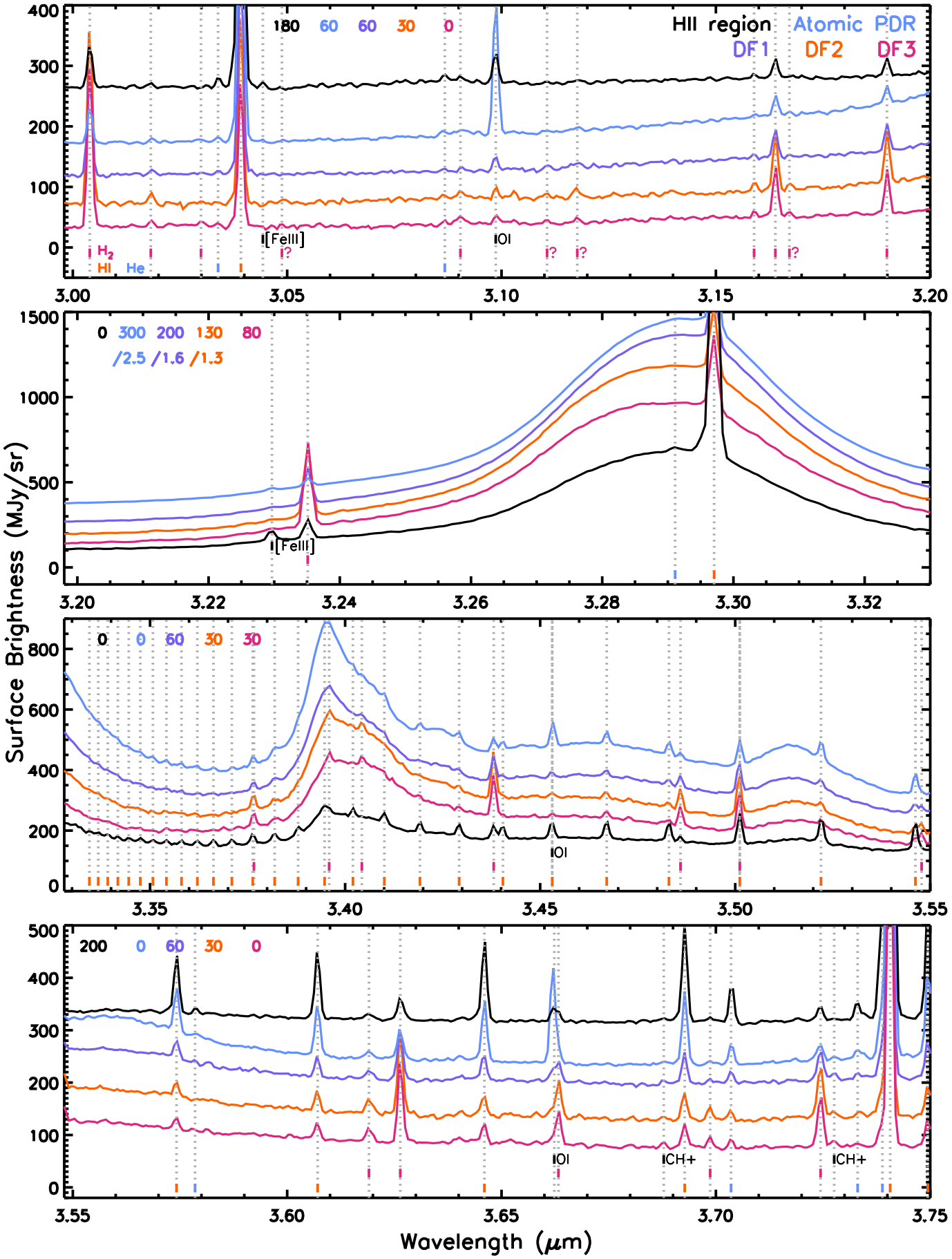

Fig. B.1. continued.

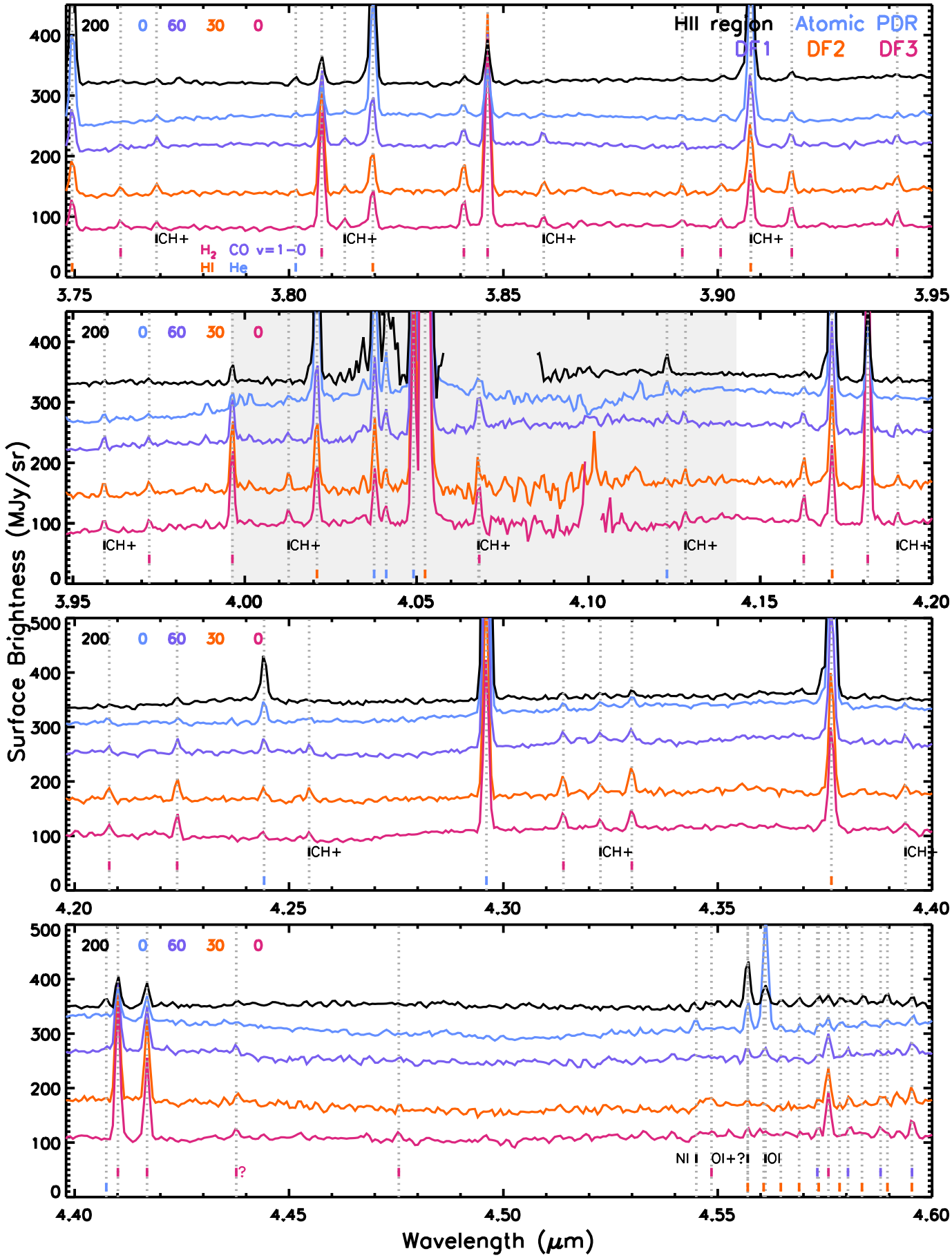

Fig. B.1. continued.

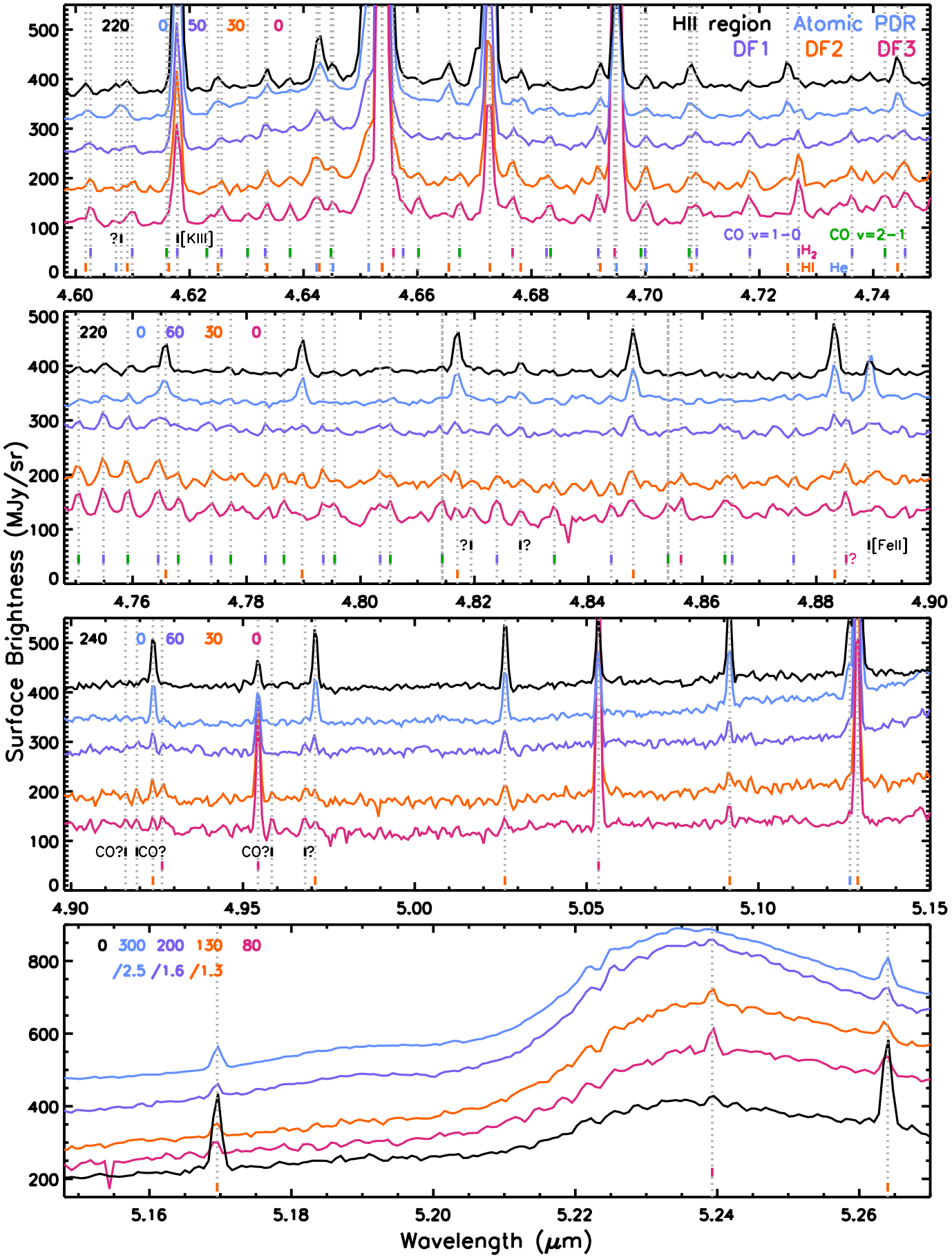

Fig. B.1. continued.

Appendix C: NIR continuum emission

We assess the behaviour of the 3 μm continuum emission by comparing its radial profile with that of Brγ and the total AIB emission (Fig. C.1). We find that the 3 μm continuum emission mimics the total AIB emission much better compared to the Brγ emission implying an origin in stochastically heated very small grains and/or blended overtone and combination bands of PAHs, consistent with previous reports (Sellgren 1984; Allamandola et al. 1989).

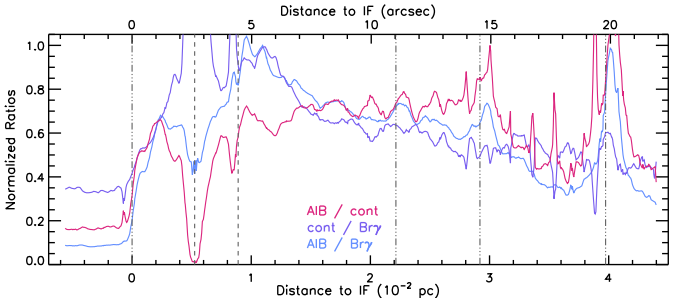

Fig. C.1. Normalised ratios of the 3 μm continuum emission, Brγ emission and total AIB emission as a function of distance to the IF (0.228 pc or 113.4″ from θ^1 Ori C) along a cut crossing the NIRSpec mosaic (see Fig. 1). As the cut is not perpendicular to the IF and distances are given along the cut, a correction factor of cos(19.58°)=0.942 needs to be applied to obtain a perpendicular distance from the IF. No extinction correction is applied. The dash-dot-dot-dot vertical lines indicate the position of the IF, DF 1, DF 2, and DF 3, respectively, from left to right. The dashed vertical lines indicated the location of the proplyds 203-504 (left) and 203-506 (right).

Appendix D: HI recombination lines

The H I recombination lines provide an estimate of the rms density in the ionised gas via:

$$I_\lambda = \frac{hc}{\lambda}\frac{3.086\times10^{18}}{4\pi}\alpha_\lambda^{eff} EM \qquad (\mathrm{erg\,cm^{-2}\,s^{-1}\,sr^{-1}}), \qquad (D.1)$$

with I_λ the intensity of the transition, α_λ^{eff} the effective recombination rate coefficient ($\mathrm{cm^3\,s^{-1}}$) and EM the emission measure ($\mathrm{cm^{-6}\,pc}$). We use α_λ^{eff} from case B recombination theory assuming an electron temperature of 10000 K and an electron density of $n_e = 1000\,\mathrm{cm^{-3}}$ (Hummer & Storey 1987).

Appendix E: [He⁺]/[H⁺] abundance

Based on the He I 1.70 μm and the H I 10-4 emission, Marconi et al. (1998) estimated the [He⁺]/[H⁺] abundance from:

$$\frac{F(\mathrm{He\,I}\,1.70\,\mu\mathrm{m})}{F(\mathrm{H\,I}\,10-4)} = 3.61\frac{[\mathrm{He^+}]}{[\mathrm{H^+}]}, \qquad (E.1)$$

which is based on the model calculations of Smits (1996) and assumes that the He I 1.70 μm is only marginally affected by collisional excitations from the metastable 2^3S state as predicted by Osterbrock et al. (1992).

Appendix F: UV intensity

One can estimate the UV continuum from UV pumped emission lines present in the NIRSpec wavelength range assuming the Bar is viewed at an inclination angle with respect to the line of sight. The O I $3d\,^3D^o - 3p\,^3P$ 1.129 μm and O I $4s\,^3S^o - 3p\,^3P$ 1.317 μm emission result from UV pumping by photons of 1027 and 1040 Å respectively. Hence, their UV intensity can be determined with:

$$I_\nu^{UV} = \frac{4\pi\sin(i)}{A f_b}\frac{\lambda_{\mathrm{IR}}\lambda_{UV}}{cW_\lambda} I(IR) \qquad (\mathrm{erg\,cm^{-2}\,s^{-1}\,Hz^{-1}}), \qquad (F.1)$$

where $I(IR)$ is the observed intensity of the IR line in $\mathrm{erg\,cm^{-2}\,s^{-1}\,sr^{-1}}$, i the inclination of the Bar with respect to the line of sight, W_λ the equivalent width of the UV line, $W_\lambda/\lambda_{UV} = 3.6\times10^{-5}$, f_b the branching ratio or probability of IR emission following a UV photon absorption (see Table 3 and 4 in Walmsley et al. 2000), and A equals 3 for the O I lines as their UV pumping lines are triplets with separation larger than W_λ (Marconi et al. 1998; Walmsley et al. 2000). The N I 1.2292 μm emission is due to both the $3d\,^4P - 3p\,^4S^o$ and $4s\,^4P - 3p\,^4P^o$ transitions and occurs following absorption of UV photons of 953 and 965 Å, respectively. The UV intensity can be estimated in a similar way as for the O I lines, where A equals 1 because its UV pumping lines are a singlet. However, N I has a more complex energy level diagram than O I and, thus, this estimate is less straightforward.

As this fluorescent emission originates from a narrow region in the ionisation front (see Sect. 5), the calculated UV intensity represents the UV radiation emergent from the H II region, where the PDR extinction is negligible. Hence, we only apply a foreground extinction, $exp(-\tau_{f,\lambda})$, with $\tau_{f,\lambda}$ the foreground optical depth as obtained in Sect. 6.1. We adopt an inclination i of 4° (Salgado et al. 2016) and obtain the branching ratio from Walmsley et al. (2000, their tables 3 and 4). Assuming an interstellar radiation field of $1\,G_0 = 1.6\times10^{-3}\,\mathrm{erg\,cm^{-2}\,s^{-1}}$ between 6 and 13.6 eV, corresponding to $8.7\times10^{-19}\,\mathrm{erg\,cm^{-2}\,s^{-1}\,Hz^{-1}}$, the obtained UV line intensity can be converted to a normalised UV intensity, G_0.

Applying this method to the strongest fluorescent line (O I 1.317 μm line; Figs. 10 and 11) and adopting an inclination angle i of 4°, we find that the maximum strength of the FUV radiation field, G_0, ranges between $2.2 - 7.1\times10^4$ across the IF seen in O I 1.317 μm emission (with a median value of 5.9×10^4). Marconi et al. (1998) derived a slightly smaller value for G_0 of 2.6×10^4 from their observations of the near-IR O I fluorescent lines, reflecting a slightly lower 1.317 μm intensity ($\sim1.4\times10^{-4}$ versus a median value of $\sim7.7\times10^{-4}\,\mathrm{erg\,cm^{-2}\,s^{-1}\,sr^{-1}}$ across the IF in our mosaic) measured at a slightly different position. In addition, these authors also adopted a slightly higher extinction value ($A_V = 2$ versus a median value of $A_V \sim 1.64$ here, see Sect. 6.1) and a larger inclination angle i ($\sin(i) = 0.20$ versus 0.07 here).

Appendix G: CI emission lines

The C I emission lines provide the electron temperature, T_e, and gas density, n_H. We detect the forbidden fine-structure lines from $2p\,^1D_2$ to $2p\,^3P_1$ and $2p\,^1D_2$ to $2p\,^3P_2$ at respectively 0.9827 and 0.9854 μm (Fig. B.1). We do not detect the third fine-structure line from $2p\,^1D_2$ to $2p\,^3P_0$ that has a much smaller A value. In addition, we detect the multiplets $3s\,^3P^0$ to $3p\,^3D$ at 1.0696 μm and $3p\,^3D$ to $3d\,^3F^0$ at 1.1759 μm (Fig. B.1; for wavelengths and transition probabilities, see Walmsley et al. 2000).

The observed line intensities for the templates are given in Table G.1. The C I emission in the H II region template likely originates from the background face-on PDR, whereas the C I

Table G.1. C I intensities for the five template spectra.

Wavelength (1)	$I_{Obs.}$ (2)	$g(\tau_{p,\lambda}, \tau_{f,\lambda})$ (3)	$I_{corr.}$ (4)
	H II region		
0.984	1.05±0.02	0.170	6.20±0.11
1.0696	0.28±0.02	0.203	1.41±0.12
1.1759	0.23±0.04	0.248	0.94±0.14
1.0696/1.1759	1.22±0.21		1.50±0.26
0.984/1.0696	3.69±0.32		4.41±0.38
	atomic PDR		
0.984	1.32±0.02	0.083	15.81±0.24
1.0696	0.37±0.03	0.101	3.68±0.28
1.1759	0.41±0.02	0.128	3.23±0.18
1.0696/1.1759	0.90±0.08		1.14±0.11
0.984/1.0696	3.53±0.27		4.30±0.33
	DF 1		
0.984	0.88±0.01	0.202	4.35±0.07
1.0696	0.22±0.04	0.237	0.93±0.18
1.1759	0.30±0.04	0.284	1.07±0.15
1.0696/1.1759	0.73±0.18		0.87±0.21
0.984/1.0696	3.99±0.77		4.67±0.90
	DF 2		
0.984	1.13±0.02	0.201	5.63±0.09
1.0696	0.20±0.03	0.236	0.86±0.12
1.1759	0.26±0.04	0.283	0.92±0.15
1.0696/1.1759	0.78±0.17		0.93±0.20
0.984/1.0696	5.60±0.80		6.56±0.94
	DF 3		
0.984	1.75±0.02	0.184	9.53±0.10
1.0696	0.34±0.02	0.217	1.56±0.09
1.1759	0.21±0.05	0.264	0.79±0.17
1.0696/1.1759	1.63±0.37		1.98±0.45
0.984/1.0696	5.15±0.31		6.09±0.36

Notes. Columns: (1) wavelength (μm). The 0.984 intensity is the sum of the 0.9827 and 0.9854 μm line intensities, the 1.0696 intensity is the sum of the 1.0687 and 1.0695 μm line intensities and the 1.1759 intensity is the sum of the 1.1752 and 1.1758 μm line intensities.; (2) observed intensity (10^{-4} erg cm^{-2} s^{-1} sr^{-1}); (3) $g(\tau_{p,\lambda}, \tau_{f,\lambda})$ as defined in Eq. G.1; (4) extinction corrected intensity (10^{-4} erg cm^{-2} s^{-1} sr^{-1}).

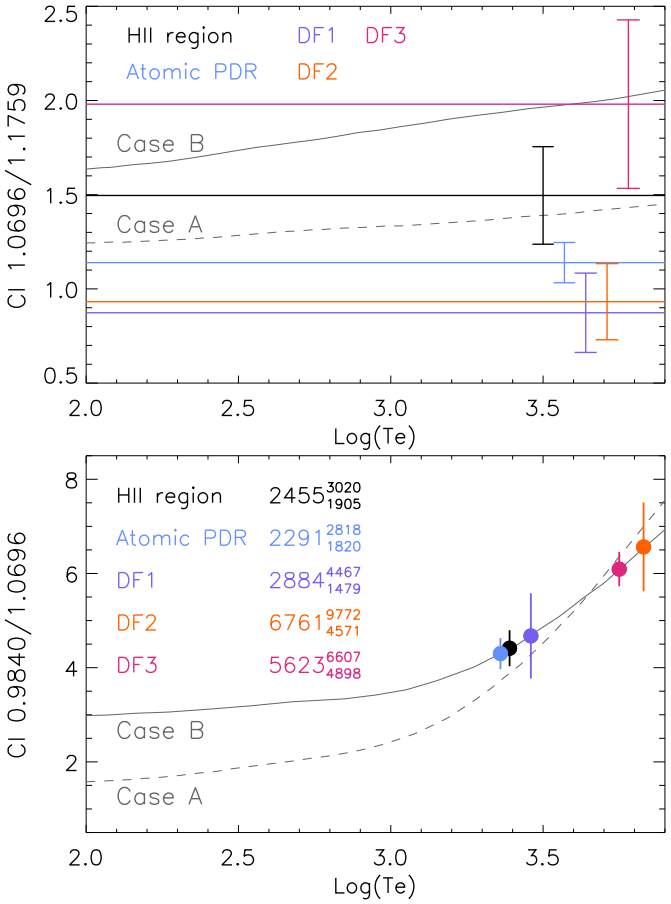

Fig. G.1. Comparison of extinction-corrected C I line ratios with computed ratios taken from Walmsley et al. (2000) that are based on calculations of Escalante & Victor (1990) for both case A and case B recombination theory. Uncertainties on the observed ratios are given by vertical lines that are placed at the derived electron temperature (lower panel) or in the [3.5 – 3.8] x-range (top panel).

emission in the atomic PDR template originates in the edge-on PDR and in the H_2 dissociation front templates it originates in the face-on PDR (see also the discussion in Sect. 5). We adopt an internal extinction of $A_V = 4$ and $A_V = 10$ for, respectively, a face-on and edge-on PDR and apply the foreground extinction derived in Sect. 6.1. The resulting extinction corresponds to:

$$g(\tau_{p,\lambda}, \tau_{f,\lambda}) = exp(-\tau_{f,\lambda}) \frac{1 - exp(-\tau_{p,\lambda})}{\tau_{p,\lambda}}, \quad \text{(G.1)}$$

with $\tau_{p,\lambda}$ and $\tau_{f,\lambda}$ the PDR and foreground optical depths at the wavelength λ, respectively.

The 1.0696/1.1759 line ratio depends primarily on the optical depth of the UV pumping line (Walmsley et al. 2000, their Fig. 14). We compare the observed intensities with their model calculations (Fig. G.1). We find that the extinction corrected 1.0696/1.1759 line ratio indicates case A conditions for the atomic PDR and case B conditions for DF 3. The ratio for the H II region can be consistent with either case A or B whereas the ratio falls below the theoretical curves for case A and B conditions for DF 1 and DF 2. Walmsley et al. (2000) also reported case A conditions based on their observations (not extinction corrected). To investigate this further, we calculate the optical depth of a resonance line (for example 1261 Å line) following Tielens (2021, eq. 4.29) assuming a typical line width of $\Delta v_{FWHM} = 3$ km/s and a neutral carbon fraction of 10^{-5}. The latter was determined using Eq. 9.6 in Tielens (2005) assuming a temperature of 1000 K, a UV radiation field G_0 of 10^4, a density of 3×10^6cm^{-3}, and a visual extinction A_V of 0. We evaluate the optical depth for two scenarios: one adopting a density $n_H = 10^5$ cm^{-3} and a line of sight depth of $L = l^{los}_{PDR} = 0.10$ pc (Sect. 6.3.2), typical values for the Bar, and one adopting a density $n_H = 10^7$ cm^{-3} and a line of sight depth of $L = 10^{-3}$ pc (e.g. Joblin et al. 2018; Goicoechea et al. 2016), typical values for dense clumps reported in the Bar. In both cases we find that the resonance line is optically thick, suggesting case B conditions. The origin of the discrepancy with the result of the 1.0696/1.1759 line ratio will be investigated in a follow-up paper. For the remainder of this analysis, we assume case B conditions.

The (0.983+0.985)/1.0696 line ratio depends primarily on the electron temperature (Walmsley et al. 2000, their Fig. 14). Adopting case B conditions, the extinction corrected line ratio corresponds to electron temperatures of approximately 2500, 2300, 2900, 6800, 5600 for the H II region, the atomic PDR,

DF 1, DF 2, and DF 3 templates respectively (Fig. G.1). Given the uncertainty in the line ratio, the derived temperatures for the H II region, the atomic PDR, and DF 1 templates are consistent with each other. Likewise, the obtained temperature for the DF 2 and DF 3 templates are consistent within their uncertainty and are surprisingly high, similar to the electron temperature of around 4700 K obtained by Walmsley et al. (2000) without correcting for extinction. No combination of foreground extinction (0-2 magn.) and internal extinction (0-15 magn.) results in an electron temperature below 1000 K for the DF 3 template (with the lowest obtained T being ~3800 K for case B).

Lastly, we can obtain an estimate of the density from the [C I] 0.984 μm intensity that is the sum of the [C I] 0.982 and 0.985 μm intensities (Walmsley et al. 2000, Eq. 2):

$$I(0.984) = I_0\, T_3^{-0.6}\, EM\, g(\tau_{p,\lambda}, \tau_{f,\lambda}) \quad (\mathrm{erg\,cm^{-2}\,s^{-1}\,sr^{-1}}), \quad \text{(G.2)}$$

with $I_0 = 6 \times 10^{-7}$ for case B (2.7×10^{-7} for case A), $T_3 = T/1000$ K, EM the carbon emission measure in $\mathrm{pc\,cm^{-6}}$ with $\mathrm{EM} = \int n_e n_{C^+} ds$. As the C I emission arises from a very thin layer of a few thousand degree gas (Sect. 6.5), we adopt A_V of 0.5 for this layer (i.e. $N = 1 \times 10^{21} \mathrm{cm^{-2}}$). Assuming all C is ionised, a C gas phase abundance of 1.6×10^{-4}, case B conditions, Eq. G.2 can be written as:

$$I(0.984) = 2.6 \times 10^{-5} \left(\frac{3000\,\mathrm{K}}{T}\right)^{0.6} \left(\frac{n}{1 \times 10^7 \mathrm{cm^{-3}}}\right) \mathrm{(erg\,cm^{-2}\,s^{-1}\,sr^{-1})}. \quad \text{(G.3)}$$

For the derived foreground extinction (Sect. 6.1), we obtain an extinction correction factor $g(\tau_{p,\lambda}, \tau_{f,\lambda})$ of 0.170, 0.083, 0.202, 0.201, 0.184 for respectively the H II region, atomic PDR, DF 1, DF 2, and DF 3 templates. This is considerably smaller than the value of ~0.3 used by Walmsley et al. (2000) who adopt $A_V = 1.5$ for the PDR extinction. We obtain an emission measure $\mathrm{EM} = A\, T_3^{0.6}$, with A being 1034±18, 2635±40, 725±11, 938±15, and 1589±17 ($\mathrm{cm^{-6}\,pc\ K^{-0.6}}$), respectively, for each of the five templates. Combined with the derived temperature, this results in an emission measure EM of 1772^{+247}_{-240}, 4334^{+602}_{-539}, 1370^{+451}_{-401}, 2953^{+790}_{-576}, 4477^{+472}_{-350} $\mathrm{cm^{-6}\,pc}$ respectively. This results in a gas density, n_H, of 2.1, 5.2, 1.6, 3.5, and $5.3 \times 10^8\ \mathrm{cm^{-3}}$ for respectively, the H II region, the atomic PDR, DF 1, DF 2, and DF 3 templates.

Appendix H: AIB emission

Appendix H.1: AIB decomposition

We have performed two spectral decompositions of the AIB emission, which are applied to every pixel of the NIRSpec mosaic and to the five template spectra. First, we employ an updated version of PAHFIT (Smith et al. 2007)[33]. In PAHFIT-based models, the AIBs are represented using Drude profiles for simplicity[34]. The continuum is fitted to the entire F290LP range (2.87–5.27 μm) using a superposition of fixed-temperature blackbody emission components and the emission lines (see Sect. 4.1) are fitted using Gaussian profiles with a FWHM that is determined by the resolution curve of F290LP. The AIB emission in the NIRSpec range is decomposed into seven components, their peak position and FWHM are listed in Table H.1. The obtained fit reproduces the observations very well (Fig. 16). The component near 3.23 μm cannot be fitted because the blue wing of the 3.29 μm feature is not reproduced well by a single Drude component (the PAHFIT model overestimates the AIB emission shortwards of 3.25 μm). On the other hand, the Drude profiles can reproduce the overlap region between the 3.29 and 3.4 μm AIBs without the requirement for an extra plateau-like component. The 3.4 μm AIB consists of two components with different widths, referred to as the '3.39' and '3.40' components. The AIB

[33] available at https://github.com/PAHFIT. We note that PAHFIT fit the spectrum expressed in μm vs. MJy/sr.

[34] An isolated harmonic oscillator would give a Lorentz profile while an electron gas without restoring force would give a Drude profile.

Table H.1. Fitting parameters used in the decomposition of the AIB emission.

PAHFIT			Gaussian decomposition		
Band	Position	FWHM	Band	Position	FWHM
(1)	(2)	(3)	(4)	(5)	(6)
3.23	3.23	0.026	3.25	3.2465	0.0375
3.29	3.291	0.03762	3.29	3.29027	0.0387
			3.33	3.32821	0.0264
3.39	3.395	0.00995	3.39	3.3944	0.0076
3.40	3.405	0.02691	3.40	3.4031	0.0216
3.42	3.4253	0.015	3.42	3.4242	0.0139
3.46	3.464	0.07012	3.46	3.4649	0.0500
3.51	3.516	0.0271	3.51	3.5164	0.0224
3.56	3.561	0.02	3.56	3.5609	0.0352
			plateau	3.4013	0.2438

Notes. Columns: (1)-(3) PAHFIT decomposition; (4)-(6) Gaussian decomposition; (1) AIB name; (2) peak position (μm); (3) FWHM (μm); (4) AIB name; (5) peak position (μm); (6) FWHM (μm).

Table H.2. Integrated intensities of the AIB components in the five template spectra (10^{-3} erg cm^{-2} s^{-1} sr^{-1}).

Band	H II region	Atomic PDR	DF 1	DF 2	DF 3
PAHFIT					
3.23	0	0	0	0	0
3.29	10.58	45.27	30.43	24.09	15.50
3.39	0.30	1.59	1.05	0.78	0.47
3.40	1.01	3.21	2.86	3.35	2.73
3.42	0.15	0.51	0.32	0.33	0.25
3.46	1.61	6.94	5.16	4.79	3.71
3.51	0.39	1.93	1.43	1.28	1.08
3.56	0.14	0.64	0.53	0.45	0
Gaussian decomposition					
3.25	0.85	3.48	2.23	1.71	1.24
3.29	6.46	28.63	18.84	14.50	9.31
3.33	0.32	1.44	1.00	0.60	0.37
3.39	0.08	0.63	0.37	0.25	0.15
3.40	0.51	1.53	1.42	1.60	1.27
3.42	0.09	0.25	0.18	0.24	0.20
3.46	0.27	1.06	0.84	0.75	0.60
3.51	0.14	0.71	0.50	0.44	0.35
3.56	0.06	0.21	0.17	0.09	0.08
plat	3.89	16.60	11.46	11.00	8.30
Deuterated PAHs[(a)]					
4.64	0.10	0.35	0.22	0.09	0.05
4.75	0.04	0.05	0.09	0.08	0.06

Notes. [(a)]See Appendix H.2 for details on the flux estimates.

emission at wavelengths longer than 3.4 μm consists of a very broadband at 3.46 μm, with two narrower bands at 3.42 μm and 3.51 μm. There is also a noticeable weaker and broad feature at 3.56 μm, but just like the wing on the blue side of 3.29 μm, the wing on the red side of the 3.51 μm band is not fitted as well. The width and power of 3.56 μm AIB were therefore harder to determine. Second, we have employed a Gaussian decomposition of the AIB emission in the 3.2 to 3.7 μm region after subtracting a linear dust continuum emission (determined in the [2.97, 3.03] and [3.65, 3.720] μm wavelength ranges)[35]. Narrow emission lines were removed prior to fitting. We fitted the AIB emission with ten Gaussians that were highly constrained in peak position and FWHM (±0.0005 and ±0.001, respectively; Table H.1). The resulting fit reproduces the observations very well (Fig. 16). We point out that in contrast to the PAHFIT method, one Gaussian represents the underlying plateau emission and one Gaussian represents the extended red wing of the 3.29 μm AIB. The remaining components are comparable between both decomposition methods. The integrated intensity of the AIB components in the five templates for both decomposition methods are given in Table H.2.

Appendix H.2: Deuterated PAHs

While an emission band at 4.646 μm is clearly visible in the H II region, the atomic PDR, and DF 1 templates (Fig. 6), we here investigate its potential presence in the DF 2 and DF 3 templates. This is severely hampered by the detection of gas-phase CO emission in the molecular PDR (Sect. 4.1) which coincides in wavelength with the potential 4.646 μm band. We therefore fit the DF 3 template with an optically thin and optically thick LTE model of ^{12}CO and ^{13}CO to assess whether the 4.6 – 4.8 μm emission (in addition to the continuum emission) can be solely due to CO emission. The optically thin model does not provide a good fit to the data whereas the optically thick model provides a better fit to the data in terms of both the relative intensities and the density of lines. While the CO emission clearly requires more advanced modelling, this simple exercise suggests that the 4.62 – 4.68 μm and 4.71 – 4.79 μm range has additional broadband emission that is not reproduced by the CO models. Next, we extract the (asymmetric) 4.646 μm band profile from the atomic PDR template where the band is strongest. We then scale this 4.646 μm band profile to match the emission in the other templates (Fig. H.1). Given the presence of numerous emission lines in this wavelength range and the uncertainty on the continuum determination, this provides an approximate estimate of its intensity in the five templates which is an upper limit for those templates with strong CO emission. The derived intensities are given in Table H.2. We note that within the uncertainties, the band profile does not vary between the templates.

As the CO model also indicated additional emission in the 4.71 – 4.79 μm range, we applied the same method here to derive rough estimates of this broadband's intensity. In this case, we extract the band profile in the DF 1 template where it is strongest. Similar as for the 4.646 μm band, this 4.746 μm band profile is also asymmetric and, when scaled, matches the observations in all templates, albeit it is relatively very weak in the H II region and atomic PDR templates. For completeness, we give the approximate intensities of this band in Table H.2.

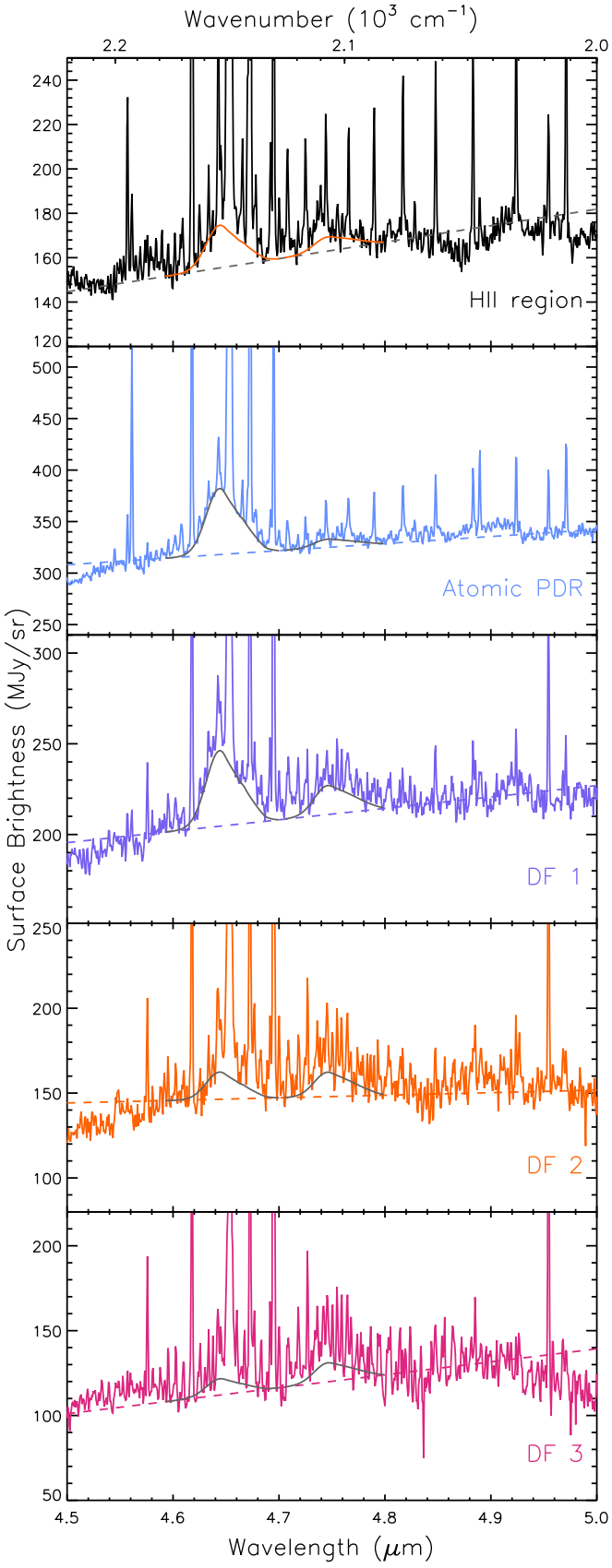

Fig. H.1. Tentative 4.644 and 4.746 μm dust features attributed to deuterated PAHs (Sect. 4.1). Local linear continua are shown by the dashed lines. The 4.646 and 4.746 μm bands are plotted on top of the continuum as a solid line. The same band profile for each feature is used for all templates. See Appendix H.2 for details.

[35] We fitted the spectrum expressed in μm vs. W m^{-2} μm^{-1} sr^{-1}.